Full Length Article

Variation in hydraulic conductivity of fractured rocks at a dam foundation during operation

Yi-Feng Chen [a,b,*], Jun Zeng [a,b], Hongtao Shi [c], Yifan Wang [a,b], Ran Hu [a,b], Zhibing Yang [a,b], Chuang-Bing Zhou [a,b,**]

[a] State Key Laboratory of Water Resources and Hydropower Engineering Science, Wuhan University, Wuhan, 430072, China
[b] Key Laboratory of Rock Mechanics in Hydraulic Structural Engineering of the Ministry of Education, Wuhan University, Wuhan, 430072, China
[c] China Three Gorges Projects Development Co., Ltd., Chengdu, 610000, China

ARTICLE INFO

ABSTRACT

Characterizing the permeability variation in fractured rocks is important in various subsurface applications, but how the permeability evolves in the foundation rocks of high dams during operation remains poorly understood. This permeability change is commonly evidenced by a continuous decrease in the amount of discharge (especially for dams on sediment-laden rivers), and can be attributed to fracture clogging and/or hydromechanical coupling. In this study, the permeability evolution of fractured rocks at a high arch dam foundation during operation was evaluated by inverse modeling based on the field time-series data of both pore pressure and discharge. A procedure combining orthogonal design, transient flow modeling, artificial neural network, and genetic algorithm was adopted to efficiently estimate the hydraulic conductivity values in each annual cycle after initial reservoir filling. The inverse results show that the permeability of the dam foundation rocks follows an exponential decay annually during operation (i.e. $K/K_0 = 0.97\mathrm{e}^{-0.59t} + 0.03$), with good agreement between field observations and numerical simulations. The significance of the obtained permeability decay function was manifested by an assessment of the long-term seepage control performance and groundwater flow behaviors at the dam site. The proposed formula is also of merit for characterizing the permeability change in riverbed rocks induced by sediment transport and deposition.

© 2021 Institute of Rock and Soil Mechanics, Chinese Academy of Sciences. Production and hosting by Elsevier B.V. This is an open access article under the CC BY-NC-ND license (http://creativecommons.org/licenses/by-nc-nd/4.0/).

1. Introduction

Characterizing the permeability of fractured rock formations is crucial to various subsurface applications, such as groundwater modeling (Chen et al., 2016a), oil and gas production (Mohamadi-Baghmolaei et al., 2016), thermal energy extraction (Sun et al., 2017), contaminant transport simulation (Carrera, 1993), hyporheic exchange characterization (Rozemeijer et al., 2010; Barlow and Coupe, 2012; Kiel and Cardenas, 2014), and optimization design of impervious barriers in dam engineering (Li et al., 2014, 2017; Chen et al., 2015). It has been well understood that the permeability of rocks is determined by the geometries (e.g. size, roughness and interconnectivity) of the void space consisting of pores and fractures through which the fluid transmits. The permeability could hence be highly anisotropic, heterogeneous, and scale-dependent (Snow, 1969), and varies with time as the flow geometries change. This could be induced by various processes such as rock deformation (Chen et al., 2007), damage (Chen et al., 2014), erosion (Sadhukhan et al., 2007), and particle clogging (Nowinski et al., 2011).

The variation in permeability of rocks induced by mechanical loading and excavation has been thoroughly investigated under both laboratory and field conditions (Chen et al., 2015). The permeability may decrease due to closure of fractures and cracks, but is more often manifested as a drastic increase (even over 2–3 orders of magnitude) due to damage growth and fracture dilation (Kelsall et al., 1984; Pusch, 1989; Souley et al., 2001). Therefore, the permeability change is typically formulated as a function of deviatoric stress (Han et al., 2016), damage variable (Chen et al.,
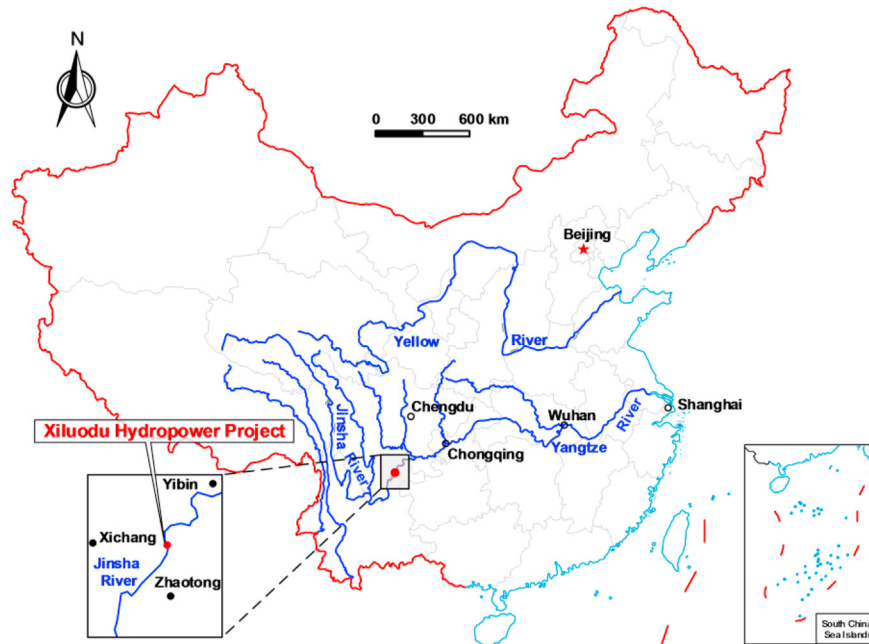
Fig. 1. Location of the Xiluodu Hydropower Project.

2014; Gao et al., 2017), irreversible strain (Chen et al., 2007; Pardoen et al., 2016), and fracture dilation (Zhou et al., 2019). An alternative pattern of permeability change in rocks is related to the migration and deposition of sediments in the fracture system, causing physical, chemical or biological clogging of flow channels (Song et al., 2007; Nowinski et al., 2011). This scenario has been frequently encountered in the vicinity of water injection boreholes (Li et al., 2019) or in the hyporheic zone of natural rivers (Datry et al., 2015; Ulrich et al., 2015). In the latter cases, fine-grained sediments (including suspension and colloid) are transported and deposited in the fractures of bedrocks (Brunke and Gonser, 1997; Brunke, 1999; Fries and Trowbridge, 2003; Packman and MacKay, 2003; Chen et al., 2008a, 2009a, b). Furthermore, it was observed that fine-grained fracture infillings could be flushed from a more permeable portion and deposited in a less permeable area (Nowinski et al., 2011). This causes significant spatial and temporal variations in rock permeability (Rehg et al., 2005; Nowinski et al., 2011; Grischek and Bartak, 2016; Mooneyham and Strom, 2018).

In hydropower engineering, dam construction and reservoir impoundment lead to sediment deposition and particle migration in the fractures of foundation rocks, especially on sediment-laden rivers. This is evidenced by the annually decreasing amount of discharge out of the drainage system at quite a number of large-scale dam sites during the operation period (e.g. Jiang and Liang, 2006; Wieland and Kirchen, 2012; Santillán et al., 2013; Shi et al., 2018). Compared to the excavation-induced permeability variation (Chen et al., 2015; Hong et al., 2017), however, how the permeability of dam foundation rocks evolves under this condition is often overlooked and rarely reported. The objective of this study is to characterize the permeability variation pattern in the foundation rocks at the Xiluodu dam site, located on the lower Jinsha River, Southwest China. Inverse modeling is performed to seek the representative hydraulic conductivity values of the foundation rocks in each annual cycle based on the groundwater observations in recent six years. Curve fitting to the inversed hydraulic conductivity values shows that the permeability of the fractured rocks at the dam

foundation follows a negative exponential function as a result of sediment deposition, fracture clogging and/or hydromechanical coupling. This relationship is of great significance for understanding the behaviors of groundwater flow and assessing the performance of seepage control in the fractured rocks at dam foundations on sediment-laden rivers.

2. Site characterization

2.1. Project description

Located on the border between Leibo County (Yunnan Province, China) and Yongshan County (Sichuan Province, China), the Xiluodu (XLD) Hydropower Project is the third-level of cascade of dams on the lower Jinsha River (Fig. 1), for the purposes of power generation, sediment trapping and flood control. The project mainly consists of a concrete double-curvature arch dam, spillway tunnels and two underground powerhouse cavern systems (Fig. 2). The arch dam has a maximum height of 285.5 m, dominated as the third highest dam of the same type in the world. The underground powerhouse cavern systems are located almost symmetrically in both sides of the river banks, each consisting of a machine hall, a transformer room, a tailrace surge chamber and hydraulic tunnels. The construction of the dam was completed in March 2014 after the river was blocked in November 2007.

2.2. Geological settings

The dam site is situated in a typical deep-incised U-shaped valley (Fan et al., 2015; Shi et al., 2018), where the Jinsha River turns $90°$ from southwest to southeast (Fig. 2). The bedrocks outcropping at the dam site are basaltic formations originating from multiple magmatic and volcanic eruption episodes (Fig. 3). The formations belong to the Emei Mountain group of the upper Permian system ($P_2\beta$), which can be categorized into 14 basalt flow layers ($P_2\beta_1–P_2\beta_{14}$) according to the eruption sequences. The rock layers mainly contain porphyritic basalt, amygdaloidal basalt, dense basalt and breccia lava, with a tuff layer of 1–5 m thick on
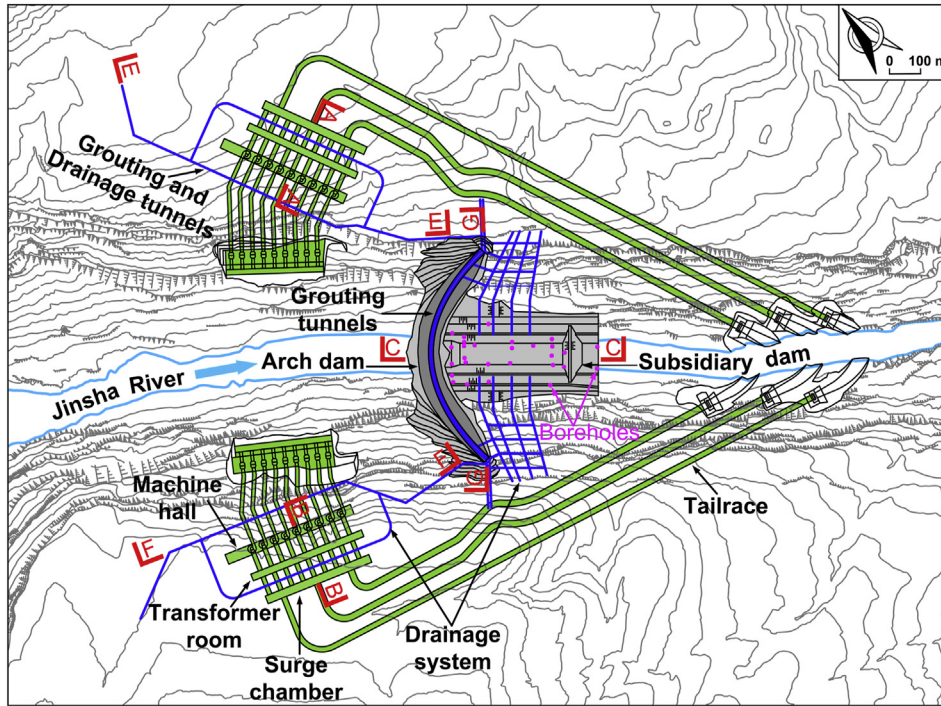
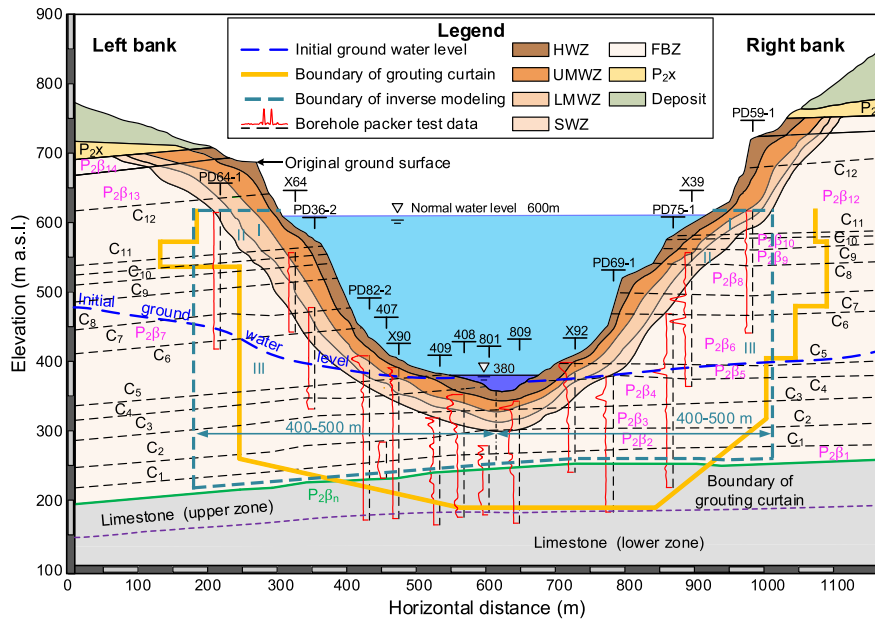**Fig. 2.** Layout of the Xiluodu Hydropower Project.

Fig. 3. Geological cross-section along the dam axis (in m).

the top of $P_2\beta_{11}$, $P_2\beta_{13}$, and $P_2\beta_{14}$, respectively. The basalt has a total thickness of 490−520 m and an orientation of N15°−50°E/ SE∠3°−24° (or N20°−40°W/NE∠4°−7° in some local places).

The basalt is underlain by the Maokou formation (P_1m) deposited in the early Permian period, which outcrops in the riverbeds about 2 km upstream the dam site and mainly consists of bioclastic limestone, with a thickness of 260−280 m. A thin clay shale layer ($P_2\beta_n$) of 2−3 m thick is deposited between $P_2\beta$ and P_1m, which is rich in illite and of lower permeability compared to the basalt and limestone. Therefore, the groundwater in the limestone formations

is confined, and the observations from outcroppings and boreholes evidenced that the upper part of the limestone has experienced significant karstification. The basalt layer $P_2\beta_{14}$ is overlain by the Xuanwei formation (P_2x) of about 97 m thick, which mainly consists of argillaceous siltstone, bauxitic claystone and carbonaceous shale. This formation is a regional aquitard, resulting in low groundwater levels in the basalt ($P_2\beta$), as shown in Fig. 3. However, influenced by the difference in landform features, the groundwater level was higher in the left bank, with a gradient of about 15%−20% discharging to the Jinsha River.

Table 1
Characteristics of critically-oriented joints at the dam site.

Set	Orientation	Spacing (m)	Length (m)	Description
1	EW/S(N)∠75°−85°	1.2−2	1.4−2.2	Closed in unweathered rocks, and rough
2	N40°−60°W/SW(NE)∠70°−80°	0.6−1.5	1−3	Mostly closed, rough, and developed in shallow depths
3	N20°−30°W/SW(NE)∠75°−82°	0.7−1.5	1.8−2.2	Closed and rough
4	N60°−80°E/SE(NW)∠65°−85°	0.8−1.2	2−4	Closed and rough
5	N20°−40°E/SE∠5°−20°	1−1.5	−	Long, closed, and smooth, more developed in the left bank
6	N15°−35°W/NE(SW)∠5°−20°	1−1.5	−	Long, closed, and smooth, more developed in the right bank

The main structures at the dam site consist of 12 gently-sloping shear zones (C_1−C_{12}) developed between the basalt layers as a result of tectonic shearing (Fig. 3). The shear zones are typically 1−2 m thick, and mainly contain basalt breccia and fragments with sizes of 0.5−3 cm. The degree of dislocation of the shear zones increases with elevation, varying from low in C_1−C_6 to medium in C_7−C_8 and to high in C_9−C_{12}. Besides the shear zones of regional continuity, local shear zones and fractures are also widely developed within each basalt layer. The local shear zones are sub-horizontal (with dip angles between 10° and 25°), formed by shearing along the bedding joints and bedding planes. The local shear zones contain basalt breccia and fragments that are densely-compacted, and mostly have a length of 20−50 m and a thickness of 5−20 cm (in shallow depths) or 2−5 cm (in deeper depths).

Fracture statistics from the outcrops and the surfaces of the exploratory adits show that there are 6 sets of critically-oriented joints developed in the basalt, as listed in Table 1. These joint sets can be categorized into two major groups. One group is sub-horizontal (sets 5 and 6), with dip angles below 30° and developed parallel to the bedding planes. The other group is sub-vertical with dip angles over 60° (sets 1-4). This group of joints is mostly short as bounded by the shear zones and interfaces between the basalt layers; at a particular location, only one or two sets of sub-vertical joints are developed. Aperture data of the joints were also collected during site characterization, showing that the aperture of joints is mostly smaller than 0.1 mm, and roughly decreases exponentially with depth.

2.3. Permeability of rocks

A total of 1644 borehole packer tests were performed during site characterization to investigate the permeability of foundation rocks, including 1327 tests in the basalt ($P_2\beta$) and 317 tests in the limestone (P_1m). Statistical analysis of the test data (Chen et al., 2018) showed that the hydraulic conductivity K of the basalt ($P_2\beta$) follows a power decay with depth d, i.e. $K = K_0 d^{-\alpha}$, where K_0 is the hydraulic conductivity value near the ground, as shown in Fig. 4a. This implies that the hydraulic conductivity is closely related to the degree of weathering (and hence fracturing) experienced by the rocks. Down from the ground surface, the basalt can be classified into five zones in decreasing weathering degree, i.e. heavily-weathered zone (HWZ, with a horizontal depth of about 10−30 m), upper moderately-weathered zone (UMWZ, 25−60 m), lower moderately-weathered zone (LMWZ, 60−100 m), slightly-weathered zone (SWZ, 90−120 m), and fresh bedrock zone (FBZ). The geometric mean of the test data is used to represent the hydraulic conductivity of each permeability zone, as shown in Fig. 4a.

It should be noted that the packer tests could not be used to interpret the anisotropy of the permeability. It can be inferred, however, from the geological settings that the hydraulic conductivity K of the basalt is anisotropic. The component of K parallel to the bedding planes ($K_{//}$) is controlled by the sub-horizontal group of joints, local shear zones, and bedding planes, while the component perpendicular to the bedding plane ($K_\perp$) is contributed by the sub-vertical group of joints. Field characterizations and tests showed that the anisotropy ratio v, defined as $v = K_\perp / K_{//}$, varies in the range of 0.025−0.3 for the basalt and shear zones. The hydraulic conductivity values representative of the site conditions are listed in Table 2.

As shown in Fig. 4b, the permeability of the limestone (P_1m) does not exhibit a clear trend with depth. According to the test data, however, the limestone could roughly be divided into an upper zone and a lower zone (Figs. 3 and 4b). The upper zone is located within about 80 m depth from the clay shale layer ($P_2\beta_n$), where the permeability has a larger mean and variability as a result of karstification. Given the limited number of hydraulic tests in the limestone and the uncertainty associated with the development of karstified fractures and cavities, the upper-bound test value is selected to represent the permeability of the upper zone, as listed in Table 2. Furthermore, site investigations indicated that the permeability anisotropy ratio is smaller in the limestone formations than that in the overlying basaltic rocks (Table 2).
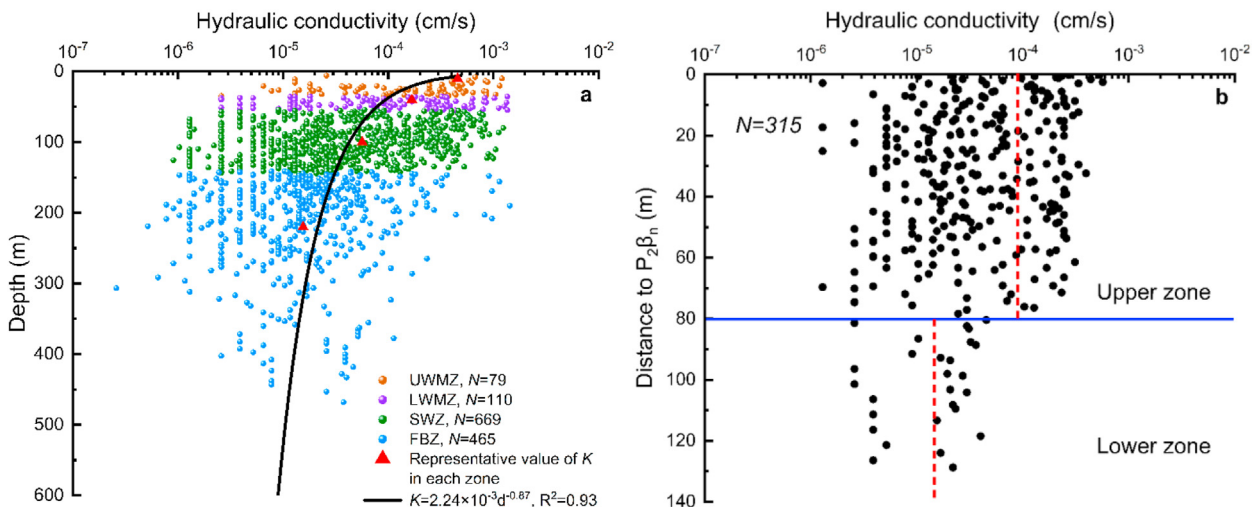
Fig. 4. Variation of hydraulic conductivity interpreted from packer tests: (a) in basaltic rocks, where the hydraulic conductivity data geometrically averaged at every 20 m-interval of depth can be well fitted with a power function, with $R^2 = 0.93$; and (b) in limestone. N is the number of test data, and R^2 is the coefficient of determination.

Table 2
Hydraulic properties of rocks at the dam site.

Material		$K_{//}$ (cm/s)	$K_{\perp}$ (cm/s)	Anisotropy ratio	Specific yield	Specific storage (m^{-1})
$P_2\beta_n$		5×10^{-6}	1×10^{-6}	0.2	0.04	4.31×10^{-6}
HWZ		1×10^{-3}	3×10^{-4}	0.3	0.1	3.72×10^{-6}
UMWZ		9×10^{-5}	2×10^{-5}	0.222	0.08	2.56×10^{-6}
LMWZ	Zone I	1×10^{-5} to 2×10^{-4}	1×10^{-6} to 4×10^{-5}	0.1–0.5	0.06	1.28×10^{-6}
	Else	3×10^{-5}	5×10^{-6}	0.167	0.06	1.28×10^{-6}
SWZ	Zone II	4×10^{-6} to 8×10^{-5}	1×10^{-6} to 1×10^{-5}	0.1–0.5	0.04	1.01×10^{-6}
	Else	1×10^{-5}	2×10^{-6}	0.2	0.04	1.01×10^{-6}
FBZ	Zone III	1×10^{-5} to 4×10^{-5}	1×10^{-7} to 5×10^{-6}	0.1–0.5	0.01	6.96×10^{-7}
	Else	3×10^{-6}	5.5×10^{-7}	0.183	0.01	6.96×10^{-7}
Limestone	Upper zone	1.2×10^{-3}	6×10^{-4}	0.5	0.1	2×10^{-6}
	Lower zone	2.3×10^{-5}	1.5×10^{-5}	0.652	0.01	1.2×10^{-6}
$C_1, C_2, C_6, C_{11}, C_{12}$ (left)		1×10^{-4}	2.5×10^{-6}	0.025	0.06	1.6×10^{-5}
C_3, C_4, C_5, C_7 (L)		1×10^{-3}	2.5×10^{-5}	0.025	0.06	1.6×10^{-5}
C_8, C_9, C_{10} (L)		2×10^{-3}	2.1×10^{-4}	0.105	0.06	1.6×10^{-5}
$C_1, C_2, C_3, C_4, C_5, C_6$ (right)		5×10^{-5}	1.5×10^{-6}	0.03	0.06	1.6×10^{-5}
C_7, C_8, C_9 (R)		2×10^{-3}	5×10^{-5}	0.025	0.06	1.6×10^{-5}
C_{10}, C_{11}, C_{12} (R)		4×10^{-3}	1.2×10^{-4}	0.03	0.06	1.6×10^{-5}
Mass concrete		1×10^{-7}	1×10^{-7}	1	0.002	3×10^{-7}
Grout curtain		1×10^{-6}	1×10^{-6}	1	0.003	5×10^{-7}

2.4. Seepage control and monitoring systems

To properly control the groundwater flow in the dam and underground powerhouse areas, a large-scale seepage control system consisting of grout curtains, drainage tunnels and drainage hole arrays was constructed, as shown in Figs. 2 and 3.

The grout curtains, covering an area of about 8.7×10^5 m^2 and constructed from six layers of grouting tunnels, extend downwards to the elevation of about 180 m in the dam foundation to cut off the potential leakage paths through the basaltic formations and the upper zone of the limestone. Downstream the grout curtains, a total of about 8000 drainage holes (140 mm in diameter and 10–74.5 m in length) were drilled from five layers of drainage tunnels to reduce the pore pressure in the dam foundation rocks and the surrounding rocks of the powerhouse caverns.

To assess the performance of the seepage control system, a groundwater monitoring system consisting of 123 piezometers and 52 weirs was installed at the dam site. Among them, 50 piezometers (numbered from P2-1 to P29-2) are located about 1.5 m below the concrete–rock interfaces in the dam foundation, together with 10 weirs (numbered as WE6-T, WE8-T, WE9-T, WE11-T and WE13-T in the left bank, and WE1-T, WE3-T, WE10-T, WE12-T and WE14-T in the right bank) installed in drainage tunnels near the abutment for collecting the discharges out of the drainage system (Fig. 5). Besides, there are 36 piezometers (numbered from PZ1-PL to PZ36-PL) and 18 weirs installed in the left cavern system (Fig. 6), and 37 piezometers (numbered from PZ1-PR to PZ37-PR) and 24 weirs in the right cavern system (Fig. 7), respectively.

2.5. Groundwater observations during operation

The impoundment of the reservoir started in September 2012, and the normal pool level was first attained in September 2014. The pool water level curve (Figs. 8 and 9) can thus be separated into an initial impounding stage before May 30, 2014 and a normal operation period afterwards that up to now contains six annual cycles (I–VI). During operation, the pore pressures in the foundation and surrounding rocks and the discharges from the drainage system were continuously recorded by the monitoring system. A representative subset of the measurements shows that except the fluctuations with the pool water level, the pore pressure measurements are rather stable during operation (Fig. 8). The

discharge, however, decreases annually, which occurs even at the weirs in the upper drainage tunnels (e.g. weir PGL4 located at elevation of 485 m, about 160 m above the riverbed, see Fig. 9). This phenomenon frequently occurs in high dam foundations (e.g. Jiang and Liang, 2006; Wieland and Kirchen, 2012; Santillán et al., 2013; Shi et al., 2018), and is attributed to reduction in the permeability of near-field rocks. The permeability reduction could be induced by hydromechanical coupling, sediment deposition and/or fracture clogging. Recall that the Jinsha River is a sediment-laden river with an annual suspended sediment concentration of 1.79 kg/m^3 and an average annual sediment load of 2.55×10^{11} kg (Cao et al., 2011). In 2014, the sediment deposited in the XLD reservoir was about 6.19×10^{10} kg, with a high trapping ratio of about 90.7% (Li et al., 2018). Therefore, fracture clogging by fine-grained sediments may dominate, as evidenced by the discharge decrease at high elevations. The purpose of this study is exactly to clarify how the permeability of the near-field rocks evolves based on the field measurements during operation.

3. Methods

3.1. Transient flow model

Given the scale and complexity of the problem and the fracture system in the study area, we assumed that the continuum approach applies for groundwater flow modeling. This assumption is acceptable for groundwater flow in dam areas, due to fully deterministic upstream and downstream boundary conditions that largely determine the hydraulic gradient in the foundation rocks, and the construction of grout curtains that weaken the role of individual fractures in groundwater flow (e.g. Zhou et al., 2015; Chen et al., 2016b). In the framework of continuum approach, the mass balance equation for transient flow in fractured rocks in any domain Ω (including its dry subdomain) can be written as (Chen et al., 2011):

$$(1 - H)S_s\frac{\partial \phi}{\partial t} + \nabla \cdot \boldsymbol{v} = 0 \tag{1}$$

where ϕ is the total water head; S_s is the specific storage; H is a Heaviside function defined as $H = 0$ if $\phi \geq z$ and $H = 1$ if $\phi < z$, in which z is the vertical coordinate; t is the time; and $\boldsymbol{v}$ is the Darcy velocity defined as
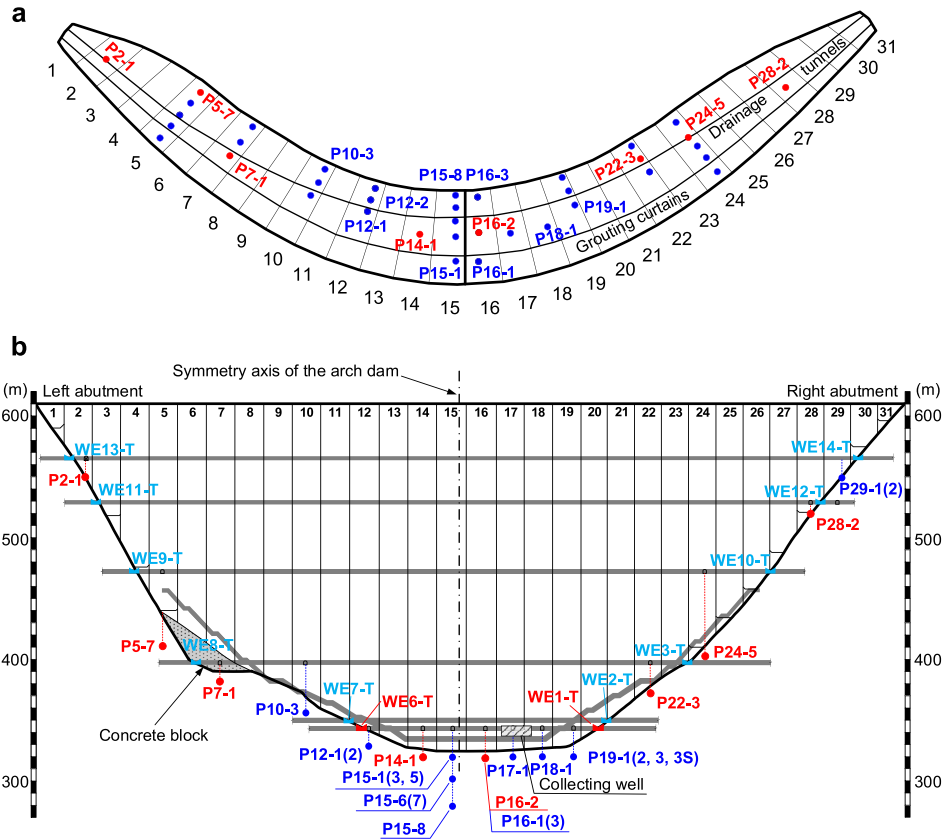
Fig. 5. Layout of piezometers and weirs deployed in the dam foundation (section G–G): (a) top view, and (b) upstream view. The numbers in red denote the monitoring points selected for inverse modeling.
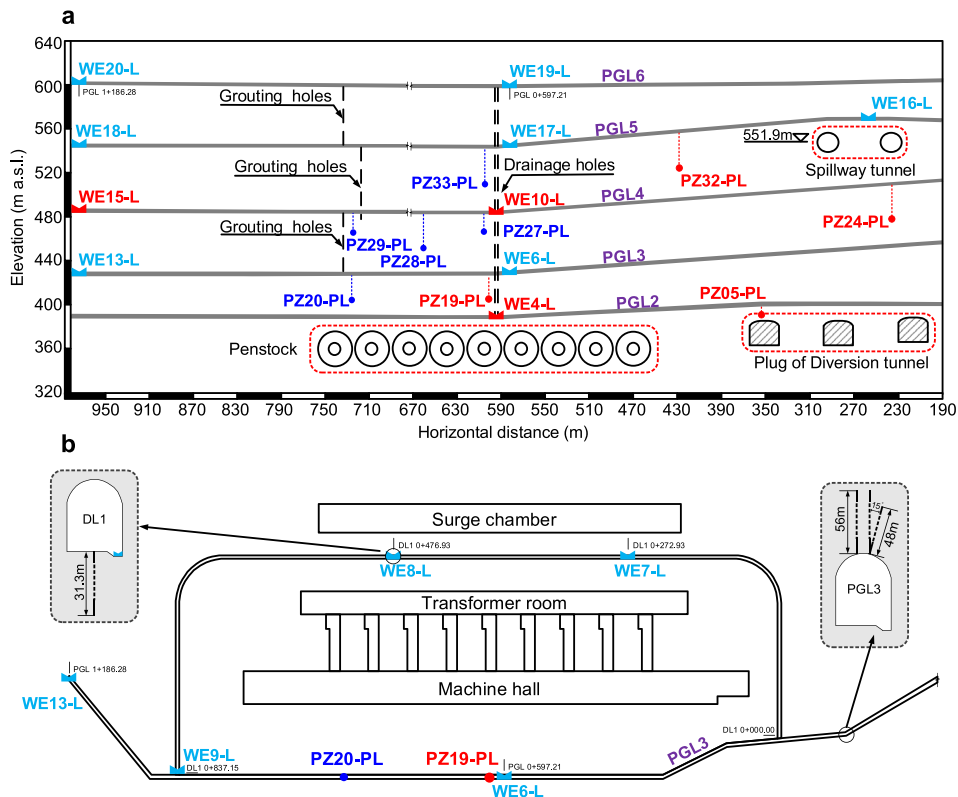

Fig. 6. Layout of piezometers and weirs deployed around the left bank caverns: (a) view along section E–E, and (b) view at elevation 425 m. The numbers in red denote the monitoring points selected for inverse modeling.
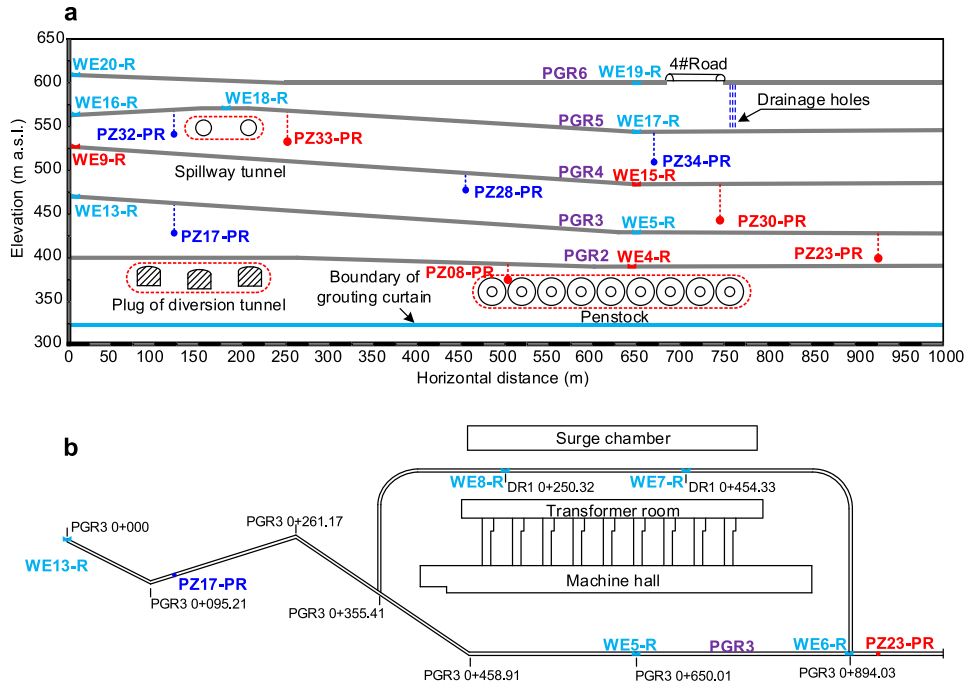
Fig. 7. Layout of piezometers and weirs deployed around the right bank caverns: (a) view along section *F–F*, and (b) view at elevation 425 m. The numbers in red denote the monitoring points selected for inverse modeling.
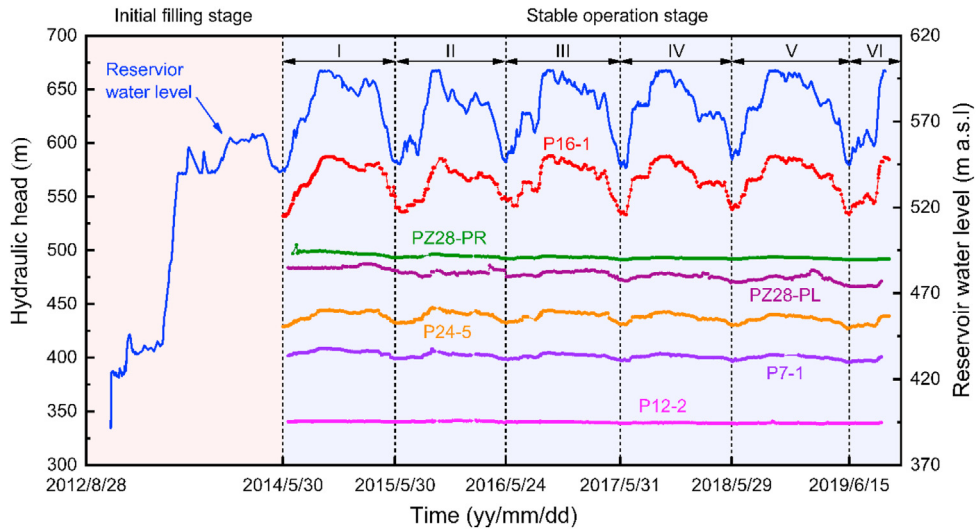

Fig. 8. Hydraulic head measurements recorded by some representative piezometers during operation.

$$\boldsymbol{v} = -(1-H)\boldsymbol{K}\nabla\phi \tag{2}$$

where $\boldsymbol{K}$ is the hydraulic conductivity tensor.

The continuity equation (Eq. (1)) is subjected to the following initial condition (Eq. (3)) and boundary conditions (Eqs. (4a)–(4d)):

$$\phi(t_0) = \overline{\phi}_0 \ (\text{in } \Omega) \tag{3}$$

$$\phi(t) = \overline{\phi} \ (\text{on } \Gamma_\phi) \tag{4a}$$

$$q_{\mathrm{n}}(t) = -\boldsymbol{n}\cdot\boldsymbol{v} = \overline{q} \ (\text{on } \Gamma_q) \tag{4b}$$

$$\phi \le z, q_{\mathrm{n}} \le 0, \ (\phi-z)q_{\mathrm{n}} = 0 \ (\text{on } \Gamma_{\mathrm{s}}) \tag{4c}$$

$$\phi = z, \ \ q_{\mathrm{n}} = -\boldsymbol{n}\cdot\left(\mu\frac{\partial\phi}{\partial t}\boldsymbol{e}_z\right) \ \left(\text{on } \Gamma_{\mathrm{f}}\right) \tag{4d}$$

where $\overline{\phi}_0$ is the initial distribution of water head, $\overline{\phi}$ is the prescribed water head on the water head boundary Γ_ϕ, $\overline{q}$ is the prescribed flux
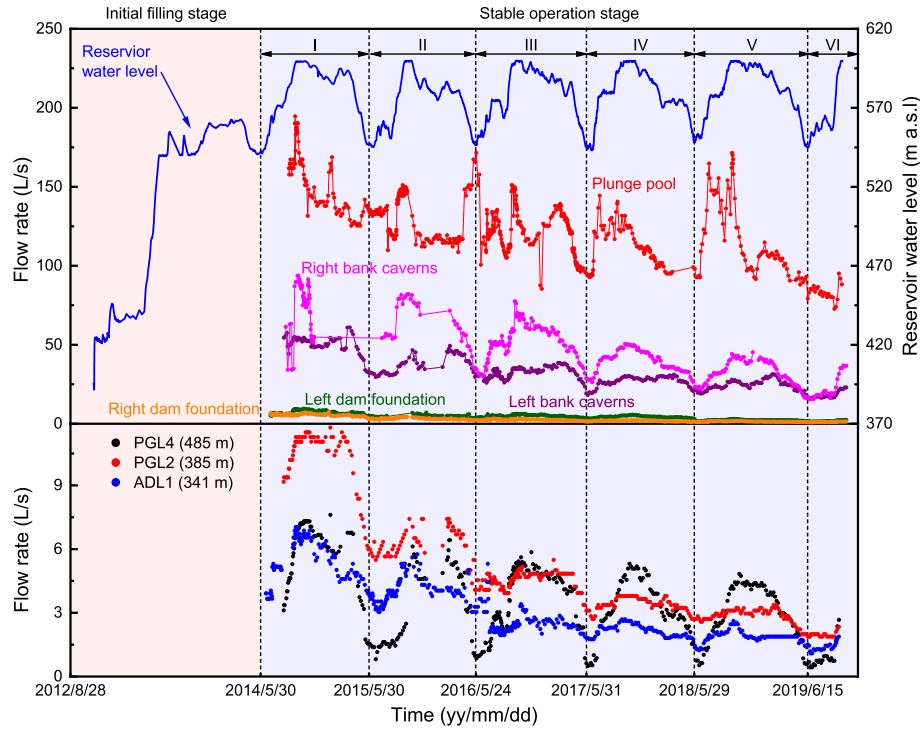
Fig. 9. Discharge measurements recorded at some representative weirs during operation. The upper plot shows the total discharges in different areas at the dam site.

on the flux boundary Γ_q, Γ_s is the potential seepage surface, Γ_f is the free surface (an interface between the wet and dry subdomains), $\boldsymbol{n}$ is the outward unit vector to the boundary, $\boldsymbol{e}_z$ is the upwards vertical unit vector, and μ is the specific yield.

The above model of transient flow with free and seepage surfaces can be effectively addressed with the discretized parabolic variational inequality formulation (Chen et al., 2011). The computer code, THYME3D, which has been developed and validated for over
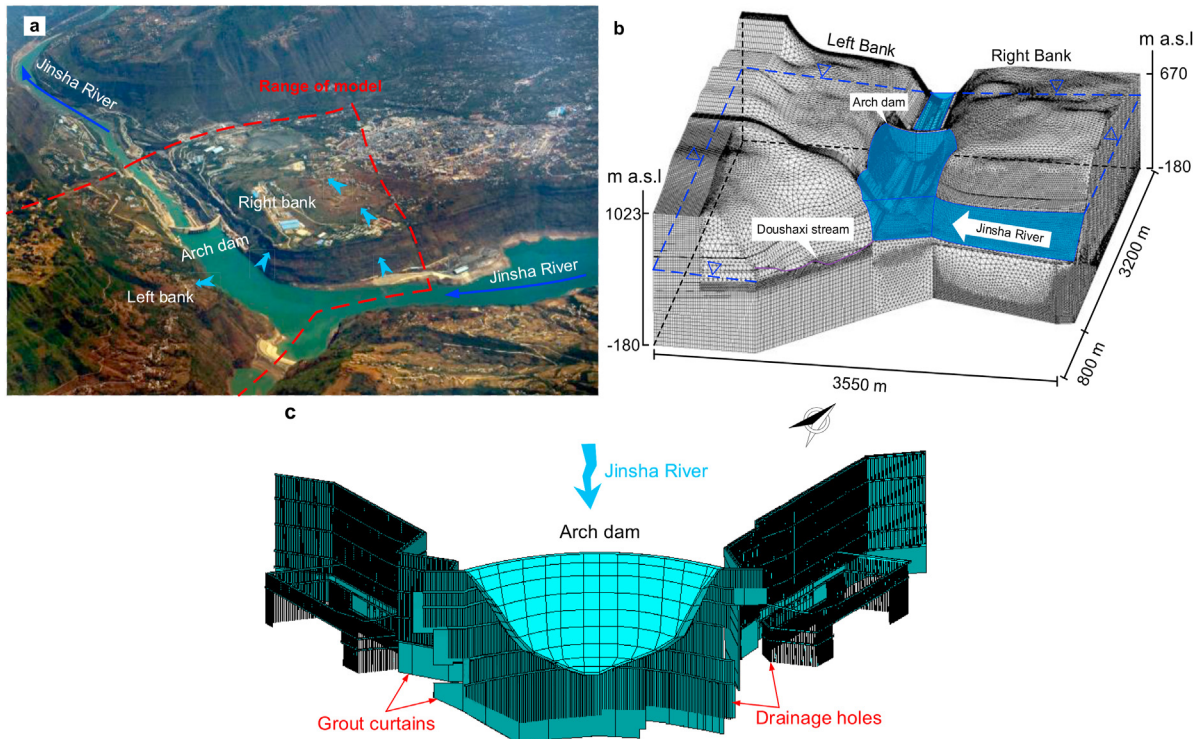

Fig. 10. Finite element model for transient flow and inverse modeling: (a) range of the domain, (b) 3D finite element mesh, and (c) seepage control system represented in the finite element model, which contains grout curtains covering an area of 866,672 m^2 and 7980 drainage holes, together with a series of grouting and drainage tunnels.

10 years (Chen et al., 2009c, 2011), is adopted for flow simulations in this study.

3.2. Finite element model and boundary conditions

A large-scale three-dimensional (3D) finite element mesh was created for flow simulations and inverse modeling at the dam site, which contains 10.8 million brick elements (with some of them degenerated to tetrahedral elements) and 3.6 million nodes, as shown in Fig. 10. The size of the model domain (Fig. 10a) is 4000 m along the river flow direction, 3550 m along the dam axis, and about 1000 m in height. The hydraulic structures (e.g. the arch dam, subsidiary dam, hydraulic tunnels, and underground powerhouse caverns) and the topographic and geological settings (e.g. the strata, permeability zones, and shear zones) were well represented (Fig. 10b). The complex seepage control system consisting of drainage and grouting tunnels, grout curtains, and drainage holes (7980 in total) was also well modeled (Fig. 10c), particularly by using a substructure technique for the drainage holes to reduce the difficulties in mesh generation (Chen et al., 2008b).

The boundary conditions were specified as follows:

(1) The time-variant pool water level was prescribed on the upstream surface of the dam and the ground surface submerged in the reservoir, and the downstream water level was controlled by the elevation of the subsidiary dam (385 m) and the river channel (about 380 m).
(2) The surfaces of the drainage tunnels and holes were prescribed as the potential seepage boundary, except the drainage holes drilled downwards in the lowest level of drainage tunnels which might become a water head boundary determined by the floor elevation of the connected drainage tunnels.
(3) The base of the model and the lateral boundary on the right-bank mountain side were assumed to be impermeable according to the site conditions.
(4) Influenced by the Doushaxi stream (Fig. 10b), the groundwater level on the left-bank mountain side was relatively high (Fig. 3), and its distribution was assumed to follow a modified trigonometric function from upstream to downstream (Chen et al., 2016b).

3.3. Inverse modeling approach

3.3.1. Parameters to be estimated

The hydraulic parameters in the transient flow model include the hydraulic conductivity tensor $\boldsymbol{K}$ (or its principal values $K_{//}$ and $K_{\perp}$), the specific storage S_s, and the specific yield μ. The specific storage and specific yield can be estimated from the compressibility and porosity of fractured rocks (note that the latter takes the sum of the porosity of intact rocks determined in laboratory and the volume fraction of fractures estimated in the field), respectively (Chen et al., 2020), as listed in Table 2. The hydraulic conductivity values of the rock formations (or zones) less influenced by excavation and hyporheic transport were determined by the packer tests (Table 2). The near-field rocks where fracture clogging most likely occurs are in the LMWZ, SWZ and FBZ (hereafter marked as zones I, II and III, respectively) below the normal pool level (i.e. 600 m) and upstream the grout curtains (Fig. 3). It is noted that the HWZ and UMWZ were mostly excavated during construction, and the range of zone III is empirically estimated to be within a horizontal distance of 400–500 m from the river (Fig. 3, basically consistent with the range of grout curtains), given that such a zone may vary from tens of meters to even several kilometers (Harvey et al., 1996; Mertes, 1997).

Consequently, the hydraulic conductivities of these three zones are chosen for inverse modeling, constituting a vector $\boldsymbol{P} = \{K_I, v_I, K_{II}, v_{II}, K_{III}, v_{III}\}$ of six unknowns, where K_i and v_i ($i =$ I, II, III) denote the component parallel to bedding planes and the anisotropy ratio of hydraulic conductivity in rock zone i, respectively.

3.3.2. Objective function

An objective function is constructed to ensure a best fit between the field measurements and numerical results, which uses the time-series of both discharge and pore pressure data to improve the reliability of the inversed results (Zhou et al., 2015; Chen et al., 2016b):

$$\min f = \left(\sum_{i=1}^{M} \frac{\|\phi_i(\boldsymbol{P}) - \tilde{\phi}_i\|_2^2}{\|\tilde{\phi}_i\|_2^2} \right)^{\frac{1}{2}} + w \left(\sum_{j=1}^{N} \frac{\|\boldsymbol{Q}_j(\boldsymbol{P}) - \tilde{\boldsymbol{Q}}_j\|_2^2}{\|\tilde{\boldsymbol{Q}}_j\|_2^2} \right)^{\frac{1}{2}} \tag{5}$$

where $\boldsymbol{P}$ is the vector of parameters to be estimated; M and N are the numbers of piezometers and weirs, respectively; φ_i and $\tilde{\varphi}_i$ are

Table 3
Locations of monitoring points selected for inverse modeling.

Monitoring point		Elevation (m)	Description
Piezometer	P2-1	551.14	Foundation of #2 dam section, in drainage tunnel ADL5 (Fig. 5)
	P5-7	409.1	Foundation of #5 dam section, downstream the arch fillet (Fig. 5)
	P7-1	387.25	Foundation of #7 dam section, downstream the grout curtain (Fig. 5)
	P14-1	322.5	Foundation of #14 dam section, downstream the grout curtain (Fig. 5)
	P16-2	320.58	Foundation of #16 dam section, downstream the grout curtain (Fig. 5)
	P22-3	367.53	Foundation of #22 dam section, downstream the drainage tunnel (Fig. 5)
	P24-5	405.81	Foundation of #24 dam section, in drainage tunnel ADR3 (Fig. 5)
	P28-2	522.37	Foundation of #28 dam section, downstream the grout curtain (Fig. 5)
	PZ-05-PL	392.58	Left-bank caverns, at chainage 0 + 353.4 m of tunnel PGL2 (Fig. 6)
	PZ-19-PL	407.67	Left-bank caverns, at chainage 0 + 604.1 m of tunnel PGL3 (Fig. 6)
	PZ-24-PL	481.1	Left-bank caverns, at chainage 0 + 243.8 m of tunnel PGL4 (Fig. 6)
	PZ-32-PL	526.13	Left-bank caverns, at chainage 0 + 431.0 m of tunnel PGL5 (Fig. 6)
	PZ-08-PR	378.3	Right-bank caverns, at chainage of 0 + 503.2 m of tunnel PGR2 (Fig. 7)
	PZ-23-PR	401	Right-bank caverns, at chainage of 0 + 926.0 m of tunnel PGR3 (Fig. 7)
	PZ-30-PR	443.5	Right-bank caverns, at chainage of 0 + 741.9 m of tunnel PGR4 (Fig. 7)
	PZ-33-PR	538.3	Right-bank caverns, at chainage of 0 + 253.5 m of tunnel PGR5 (Fig. 7)
Weir	WE1-T	341	Dam foundation, in drainage tunnel ADR1 (Fig. 5)
	WE6-T	341	Dam foundation, in drainage tunnel ADL1 (Fig. 5)
	WE4-L	385	Left-bank caverns, in tunnel PGL2 (Fig. 6)
	WE10-L	485	Left-bank caverns, for chainage 0 + 000 m to 0 + 597.21 m of PGL4 (Fig. 6)
	WE15-L	485	Left-bank caverns, for chainages from 0 + 597.21 m to 1 + 186.28 m of PGL4 (Fig. 6)
	WE4-R	385	Right-bank caverns, in tunnel PGR2 (Fig. 7)
	WE9-R	485	Right-bank caverns, for chainage 0 + 000 m to 0 + 650.01 m of PGR4 (Fig. 7)
	WE15-R	485	Right-bank caverns, for chainages from 0 + 650.01 m to 1 + 099.89 m of PGR4 (Fig. 7)

the time-series of calculated and measured water heads (or pore pressures) at piezometer i, respectively; Q_j and $\tilde{Q}_j$ are the time-series of calculated and measured discharges at weir j, respectively; w is a weight coefficient introduced to ensure a balance between the relative errors of pore pressure and discharge measurements; and $\|\cdot\|_2$ denotes the Euclidean norm of a vector.

The measurement data in Eq. (5) need to be properly selected by taking into account the layout of the monitoring system, so that the groundwater flow behaviors could be well represented. In this study, a total of 16 piezometers and 8 weirs are selected for inverse modeling (Table 3), which accounts for 13%–15% of the total number of piezometers and weirs at the site. The weight coefficient takes $w = 0.07$ in this study.

3.3.3. Inverse modeling procedure

The inverse modeling started on May 30, 2014, due to lack of measurements before that time; it was performed annually based on the measurements collected in each annual cycle (see Figs. 8 and 9). To address this large-scale inverse problem, the procedure combining orthogonal design (OD), finite element analysis, artificial neural network (ANN) and genetic algorithm (GA) (Zhou et al., 2015; Chen et al., 2016b, 2020; Hong et al., 2017) was adopted in this study. The OD yields a representative set of 36 parameter combinations by constructing an orthogonal table $L_{36}(6^6)$, with 6 parameters to be estimated (i.e. $|P| = 6$) and 6 levels specified for

each parameter from the ranges empirically given in Table 2. Forward modeling of transient flow is then invoked by using each of the parameter combinations as input parameters, hence drastically reducing the computational cost of the finite element simulations. The numerically obtained time-series data at the monitoring points (as output), together with the parameter combinations and the prescribed water head boundary conditions (as input), are used to construct and train a back propagation neural network (BPNN) model, having a structure of 6-27-23-20 neurons from input to output layers. A GA, with a size of 100 for the initial population and probabilities of 0.9 and 0.1 for crossover and mutation operations, respectively, is finally used to obtain a globally optimal estimate of P by minimizing Eq. (5) with the numerical data output by the BPNN model. Details of the algorithm can be found in Chen et al. (2020).

4. Results

4.1. Variation of hydraulic conductivity

The inversed values of hydraulic conductivity in each annual cycle for the near-field rock zones influenced by sediment transport (possibly with other factors) are shown in Fig. 11. It is interesting to observe that the inversed K values (hereafter referred to as the component parallel to bedding planes) in the first annual cycle (i.e.
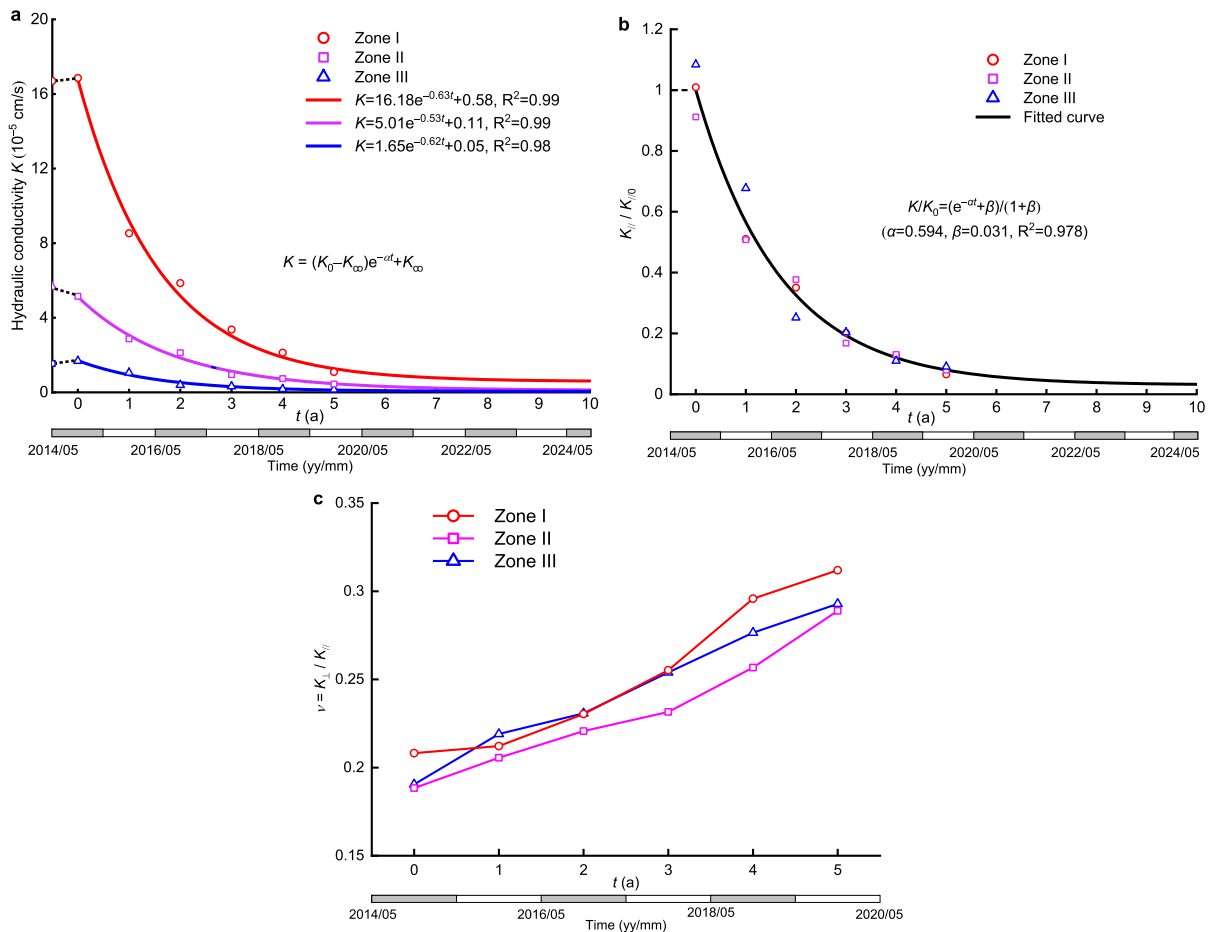

Fig. 11. The annually inversed hydraulic conductivity values in the near-field rocks: (a) The component of K parallel to bedding planes, $K_{//}$, where the data points plotted on the vertical axis denote the representative values of hydraulic conductivity determined from site investigation data; (b) The $K_{//}$ component normalized by its initial value $K_{//0}$ estimated in the first year of operation, $K_{//}/K_{//0}$; and (c) The anisotropy ratio, $K_{\perp}/K_{//}$.

K_0) are rather close to the site characterization values estimated from packer tests, as plotted in Fig. 4a. This indicates that the permeability increase induced by excavation during construction has been compensated by the permeability decrease induced by fracture clogging during the initial impoundment and operation before May 2015. From then on, the permeability of the near-field rocks decays annually, which could be best-fitted with the following negative exponential function (Fig. 11a):

$$K = (K_0 - K_\infty)e^{-\alpha t} + K_\infty \tag{6}$$

where t is the time in year, K_0 is the inversed K value in the first annual cycle (marked by $t = 0$), K_∞ is the asymptotic K value after a sufficient long time, and α is a coefficient denoting the decay rate of permeability.

Fig. 11b shows that the normalized permeability, defined as K/K_0, follows a unified exponential decay for all the three near-field rock zones:

$$\frac{K}{K_0} = \frac{e^{-\alpha t} + \beta}{1 + \beta} \tag{7}$$

where β is a coefficient in the form of $\beta = K_\infty/(K_0 - K_\infty)$. The curve-fitting yields $\alpha = 0.594$ and $\beta = 0.031$ in this study, with $R^2 \geq 0.98$. This high coefficient of determination results from the clear trend of decrease in discharges at the site, and from the proper choice of monitoring points in the inverse modeling as well. Sensitivity analysis shows that the permeability of rock zones II and III is most sensitive to the discharges in tunnels PGL4 and PGR4 (485 m) and to the discharges in tunnels PGL2 and PGR2 (385 m), respectively.

These different sensitivities make the permeability in different zones relatively easier to be tuned in back calculations.

Eq. (7) implies that after six years of operation ($t = 5$ a, recalling that the first annual cycle is marked by $t = 0$), the permeability of the near-field rocks in the dam area is reduced by one order of magnitude, and presently, the permeability variation tends to a quasi-stable state. This equation further predicts that the stable state (in terms of the permeability change, and hence the groundwater flow behavior) could be attained at $t = 9$ a (i.e. in 2024). This prediction may be of practical significance in answering when the groundwater flow-induced valley deformation (Cheng et al., 2017) tends to converge.

Fig. 11c shows the inversed anisotropy ratio values of hydraulic conductivity, ranging between 0.18 and 0.32 for the near-field rocks. It should be noted that with increase of horizontal depth (i.e. in zone III), the anisotropy ratio (in the potential range characteristic of site conditions, e.g. 0.1–0.5) becomes less sensitive to the seepage field, and hence the inversed values of ν_{III} are less reliable. Consequently, it is hard to discern a clear trend of permeability anisotropy with increasing horizontal depth (i.e. from zone I to III), but the plot indicates a slightly decreasing trend in the degree of flow anisotropy as the clogging effect accumulates from year to year.

4.2. Comparison with field measurements

Transient flow simulation had been performed in the study area for about six years since May 30, 2014, using the inversed parameters (Fig. 11) for the near-field rocks. The hydraulic parameters of other rock zones are taken from Table 2 and keep unchanged
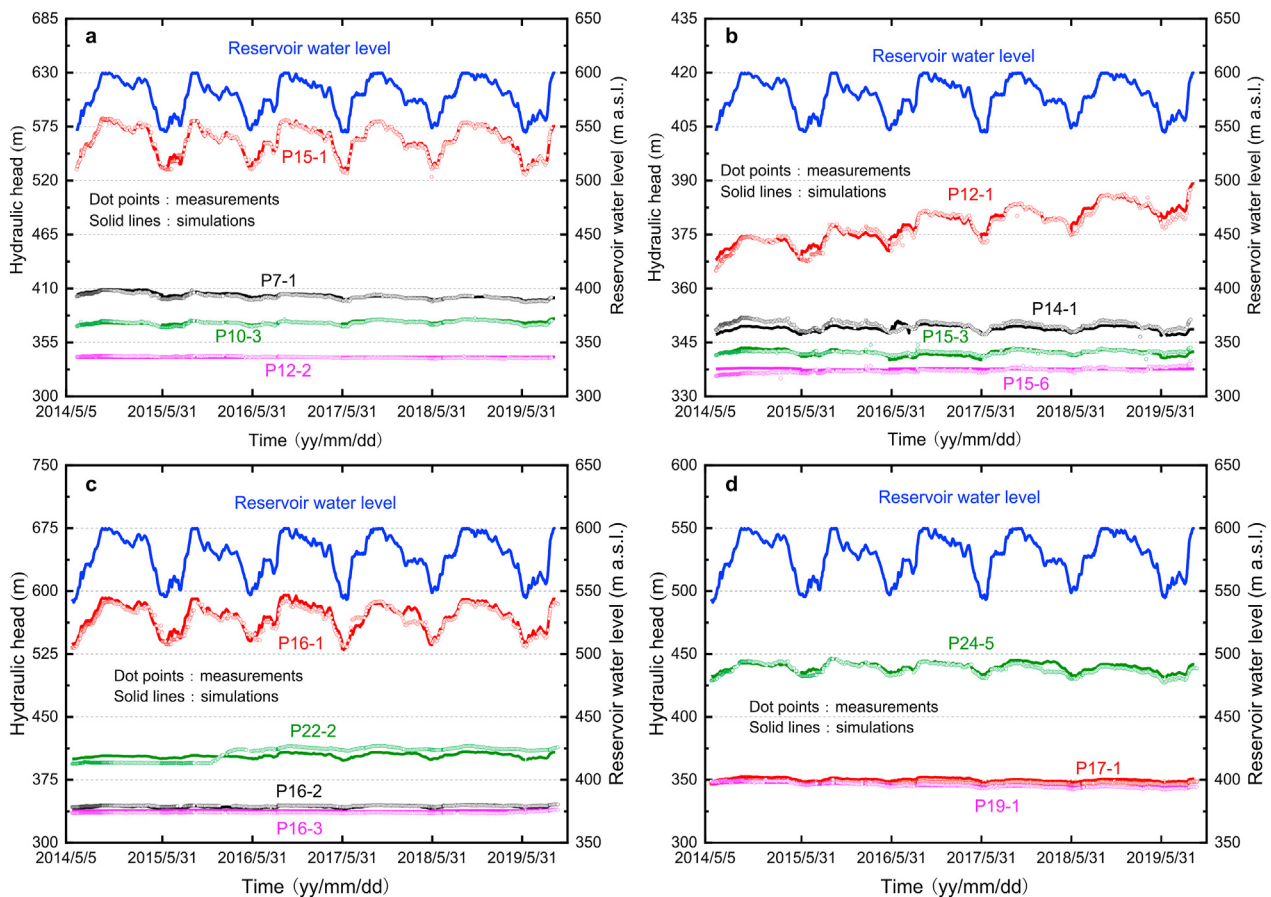

Fig. 12. Comparison between the measured and calculated time-series of hydraulic head in the dam foundation rocks.

during simulation; and the boundary conditions are specified in the same way as described in Section 3.2. The error between the obtained time-series of numerical results (R) and the measurements (Z) at any monitoring point is evaluated by the following three widely-applied statistical criteria (e.g. Tseng et al., 2001; Jain and Kumar, 2007):

$$MAE = \frac{1}{N} \sum_{i=1}^{N} |R_i - Z_i| \tag{8a}$$

$$RMSE = \sqrt{\frac{1}{N} \sum_{i=1}^{N} (R_i - Z_i)^2} \tag{8b}$$

$$MAPE = \frac{1}{N} \sum_{i=1}^{N} \left| \frac{R_i - Z_i}{Z_i} \right| \tag{8c}$$

where MAE is the mean absolute error; $RMSE$ is the root mean square error; $MAPE$ is the mean absolute percent error; R_i and Z_i are the numerically obtained and measured data at time point i, respectively.

Figs. 12 and 13 show the evolution of calculated and measured hydraulic heads (converted from pore pressures) at 29 piezometers, including 15 piezometers in the dam foundation rocks (Fig. 5), and 7 piezometers in the surrounding rocks of each cavern system

(Figs. 6 and 7), respectively. A comparison between the curves shows that the numerical simulation well reproduces the pore pressure variations, except for some local fluctuations (e.g. at piezometer PZ33-PL). The MAE, $RMSE$ and $MAPE$ errors are 0.48–8.14 m, 0.23–9.92 m and 0.12%–7.36%, with the means of 2.11 m, 2.92 m and 0.73%, respectively, as listed in Table 4. The largest errors occur at piezometer PZ33-PL, where seasonal fluctuations of pore pressure are not well captured, but these errors are still within the engineering accuracy. The piezometers P15-1 and P16-1 are located upstream the grout curtains, and hence have the largest readings and fluctuations of pore pressure; other piezometers are on the downstream side, and have smaller readings and narrower range of fluctuations, as remarkably influenced by the drainage system. All these features are well simulated by the numerical model.

Unlike the pore pressure in the fractured rocks, the discharge from the drainage system seems to vary in a more complex form, fluctuating significantly with pool water level and exhibiting a decreasing trend annually, as plotted in Fig. 14. A comparison between the numerical results and measurements in 16 representative drainage tunnels and in the plunge pool area shows that the numerical simulation reasonably predicts both the trend and magnitude of the discharge data. The MAE, $RMSE$ and $MAPE$ errors are 0.16–4.03 L/s, 0.08–20.74 L/s and 6.02%–81.57%, with the means of 1.35 L/s, 2.63 L/s and 24.77%, respectively (Table 5). Note that for small discharge, $MAPE$ could be high even the absolute error is negligible. For example, in tunnel PGR3, $MAPE$ is as high as
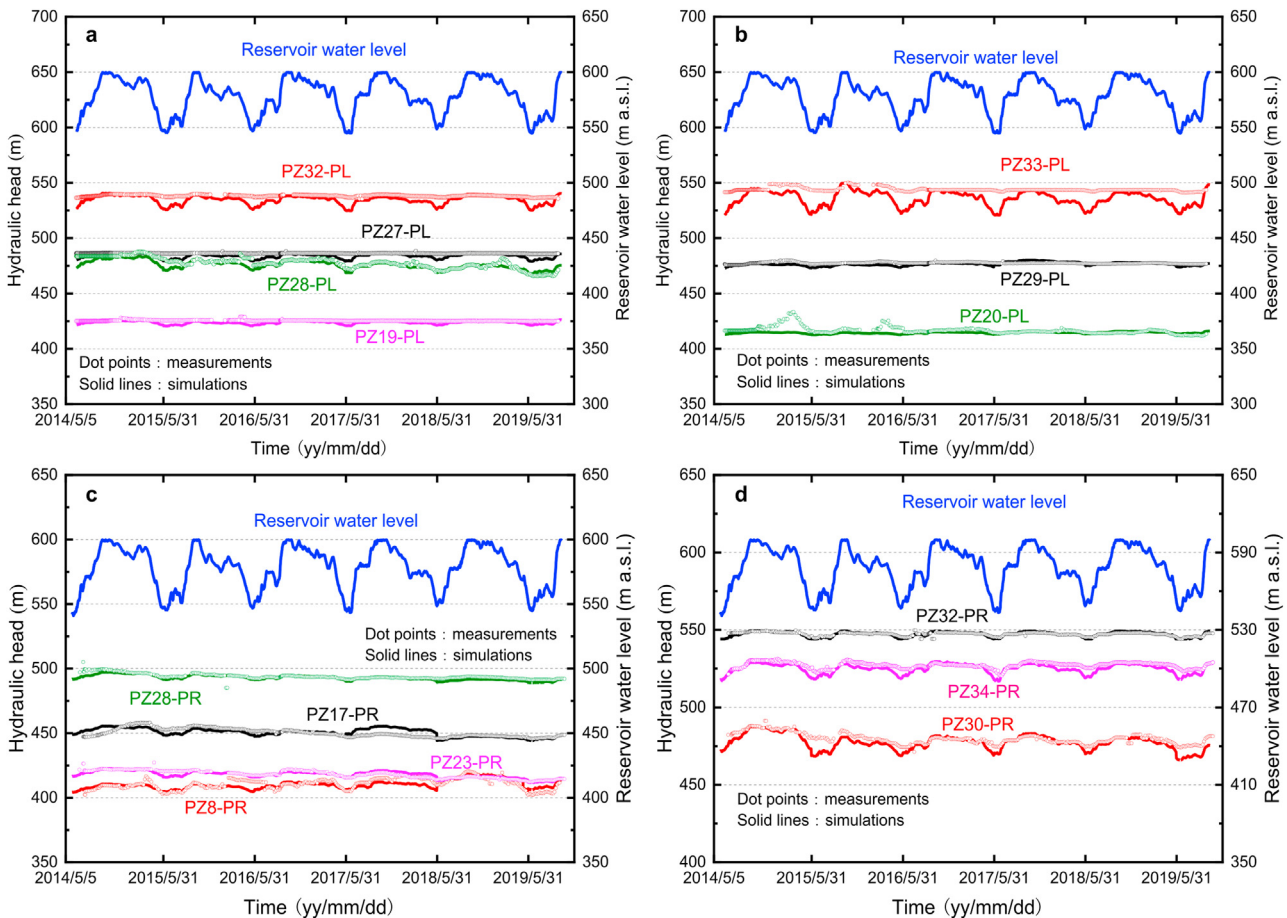

Fig. 13. Comparison between the measured and calculated times-series of hydraulic head in the surrounding rocks of the left-bank cavern system (a, b) and the right-bank cavern system (c, d).

Table 4
Errors between the measured and calculated time-series of hydraulic head at 29 typical piezometers.

Piezometer	MAE (m)	RMSE (m)	MAPE (%)	Piezometer	MAE (m)	RMSE (m)	MAPE (%)
P7-1	1.4	1.62	0.35	PZ17-PR	2.57	3.22	0.57
P10-3	1.04	1.3	0.28	PZ23-PR	1.18	1.65	0.28
P12-1	1.18	1.52	0.32	PZ28-PR	1.13	1.67	0.23
P12-2	0.91	0.99	0.27	PZ30-PR	2.8	4.32	0.59
P14-1	1.18	1.37	0.34	PZ32-PR	0.66	0.99	0.12
P15-1	1.49	2.32	0.27	PZ34-PR	2.27	2.75	0.43
P15-3	0.48	0.61	0.14	PZ19-PL	1.66	2.1	0.39
P15-6	0.96	0.23	0.78	PZ20-PL	2.58	3.91	0.61
P16-1	5.69	6.9	1	PZ27-PL	2.31	2.95	0.48
P16-2	1.94	4.23	0.58	PZ28-PL	2.48	3.39	0.52
P16-3	2.59	3.36	0.77	PZ29-PL	2.8	4.32	0.59
P17-1	2.42	2.48	0.7	PZ32-PL	1.48	1.78	0.31
P19-1	0.77	0.94	0.22	PZ33-PL	8.14	9.92	1.5
P22-2	1.82	7.77	7.36	R/M with $K(t)$	0.48–8.14, 2.11	0.23–9.92, 2.92	0.12–7.36, 0.73
P24-5	2.23	2.68	0.51	R/M with K_0	0.47–11.94, 2.87	0.56–13.62, 3.55	0.14–2.93, 0.66
PZ8-PR	2.59	3.28	0.63				

Note: R/M with $K(t)$ and R/M with K_0 denote the range and mean of hydraulic head calculation errors for the cases where the hydraulic conductivity takes the inversed values and the site characterization values, respectively.

81.57%, but the *MAE* and *RMSE* errors are acceptable (1.57 L/s and 2.22 L/s). The discharge observations in the plunge pool area fluctuate drastically, due to regular maintenance and repairs during which pumping and water injection are performed successively. Although this scenario is not considered in our simulation, the numerical results reasonably reproduce the magnitude and the evolving trend of discharge in this area (with a high *RMSE* error of 20.74 L/s but a moderate *MAPE* value of 12.55%).

Fig. 15 plots a comparison between the measured and simulated total discharges from the drainage system at the normal pool level (600 m) in early October annually, showing again that the discharge at the dam site is well modeled, with a relative error smaller than 14.3%. The range and mean errors of numerical results listed in Tables 3 and 4 indicate that when the hydraulic conductivity variation is disregarded (i.e. using the values obtained during site characterization), the predictions of discharge deviate significantly from the measurements. This justifies the need for evaluating the variation in hydraulic conductivity during operation.

4.3. Seepage flow behaviors at the site

Fig. 16 shows the hydraulic head contours and phreatic surface variations during operation in the underground powerhouse areas along cross-sections A–A and B–B (with their traces shown in Fig. 2), and Fig. 17 shows a comparison of the hydraulic head contours along the central cross-section C–C of the dam foundation in 2014 and 2019. The reservoir water level for these plots is 600 m (normal pool level) occurring in early October annually. These plots indicate that although the seepage field at the site varies from year to year, the changes in groundwater level (and hence the pore pressure) are within an acceptable small range. This evidences that the grout curtains and drainage system were well designed and constructed, and function well during operation in cutting off the flow paths or reducing the pore pressure downstream the impervious barriers.

Furthermore, the clogging effect in near-field rocks leads to slight increase in groundwater level on the upstream side of the grout curtains and moderate decrease of the maximum hydraulic

gradient in the grout curtains from 30.4 in 2014 to 20.2 in 2019. Owing to different lateral recharge conditions from the left-bank and right-bank mountain sides and influenced by the orientation of the bedding planes, the seepage fields in the left-bank and right-bank cavern areas downstream the grout curtains behave slightly different and exhibit slow trends in discharge (Fig. 16a) and recharge (Fig. 16b), respectively. But the seepage fields have approached a quasi-stable state.

The other aspect of the seepage fields worthy of attention is the discharges in different local areas. For instance, the discharge from tunnels DL1–DL3 in the left-bank cavern area is relatively large in magnitude (Fig. 14a); this is mostly caused by shear zones C_3–C_5 which intersect the tunnels and provide flow paths from reservoir and the mountain side (Fig. 16a) and by the excavation-induced permeability increase in the surrounding rocks (Chen et al., 2015). The moderate discharge from tunnels DR1–DR3 in the right-bank cavern area (Fig. 14d) is induced for the same reason (but by shear zones C_2–C_4, Fig. 16b). Interestingly, as shown in Fig. 14c, the discharge from tunnel PGR4 is much larger than those from the tunnels at lower elevation (e.g. PGR3). This results from the gently-sloping shear zones C_7 and C_8 that cut through the tunnel and the particular topographic feature in the right bank where the Jinsha River makes a 90° turn, favoring the leakage from the reservoir to the tunnel (Figs. 10a and 16b).

Another particular concern is the discharge in the plunge pool area, which accounts for over a half (45.9%–74.8%) of the total discharge at the dam site (Figs. 14e and 15). The underlying reason is that during site investigation, a total of 28 boreholes (76 mm in diameter) were drilled in this area (with their locations shown in Fig. 2), penetrating into the upper zone of the Maokou limestone, but were not properly plugged afterwards. These abandoned boreholes therefore form the channels to transmit the confined water in the limestone formation upwards to the drainage system in the plunge pool area, which has been confirmed by the observed abnormal temperature rise of the seeped water. The flow behavior of these abandoned boreholes is described by Hagen–Poiseuille's law in this study, and an equivalent diameter of 22 mm can best approximate the conductivity of these boreholes after years of clogging by riverbed sediments and blasting fragments during site investigation and construction (Zeng et al., 2019).

Therefore, all the particular phenomena of discharge at the dam site can be well interpreted with the site conditions and the inversed results. Given the extremely large scale of the project, the amount of the total discharge at the site has been satisfactorily controlled to a sufficiently small magnitude, which even decreases significantly each year due to the clogging and/or hydromechanical coupling effects in the foundation rocks (Fig. 15).

5. Conclusions

This study phenomenologically investigated the permeability variation of the fractured rocks at a high arch dam foundation induced by sediment deposition and fracture clogging (possibly together with hydromechanical coupling). This was achieved by performing inverse modeling in each annual cycle based on the time-series data of both pore pressure and discharge collected after initial reservoir filling. The inverse modeling showed that at the end of the first operation year, the permeability values of the foundation rocks are basically the same as the site characterization values before construction of the dam, implying that the excavation-induced permeability change has been compensated by fracture clogging during this initial impounding and operation stage. The permeability of the foundation rocks then decays annually, following a negative exponential function in the form of $K/K_0 = 0.97e^{-0.59t} + 0.03$ (here t is the time in year). Numerical
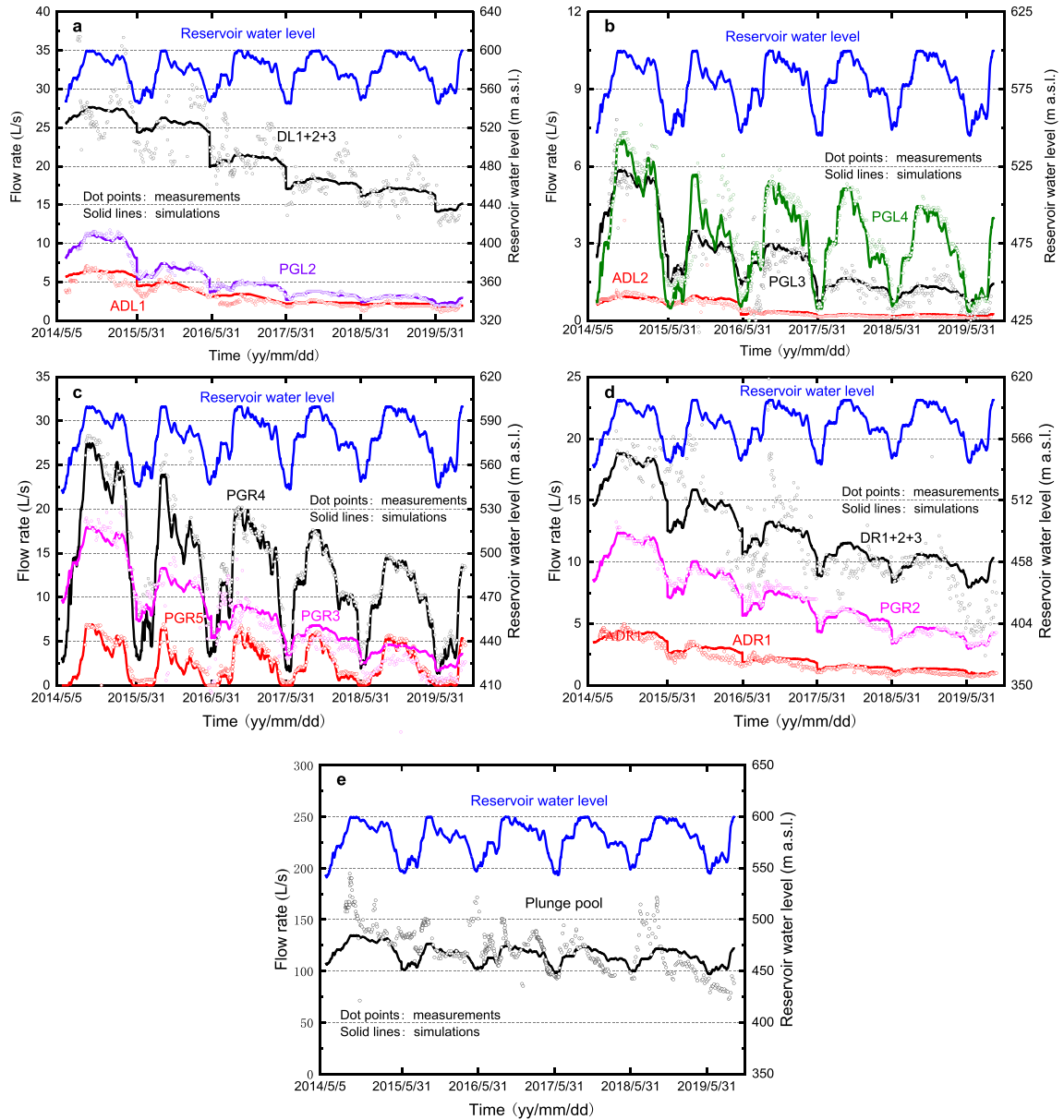
Fig. 14. Comparison between the measured and calculated time-series of discharge in the areas of the left bank (a, b), right bank (c, d), and plunge pool (e).

Table 5
Errors between the measured and calculated time-series of total discharges in 16 typical tunnels and in the plunge pool area.

Tunnel	MAE (L/s)	RMSE (L/s)	MAPE (%)	Tunnel	MAE (L/s)	RMSE (L/s)	MAPE (%)
ADL1	0.8	0.63	21.93	DR1–DR3	1.98	2.55	20.7
ADL2	0.16	0.08	21.93	ADR1	0.31	0.39	17.18
PGL2	0.41	0.27	6.02	PGR4	1.4	1.98	13.69
PGL3	0.66	0.5	66.52	PGR5	0.57	0.68	36.47
PGL4	2.56	1.89	8.58	Plunge pool	4.03	20.74	12.55
PGR2	0.55	0.42	6.33	R/M with $K(t)$	0.16, −4.03, 1.35	0.08, −20.74, 2.63	6.02−81.57, 24.77
PGR3	1.57	2.22	81.57	R/M with K_0	0.37, −8.15, 3.66	0.47, −20.81, 5.48	13.95−423.94, 126.49
DL1–DL3	2.56	1.89	8.58				

Note: R/M with $K(t)$ and R/M with K_0 denote the range and mean of discharge calculation errors for the cases where the hydraulic conductivity takes the inversed values and the site characterization values, respectively.
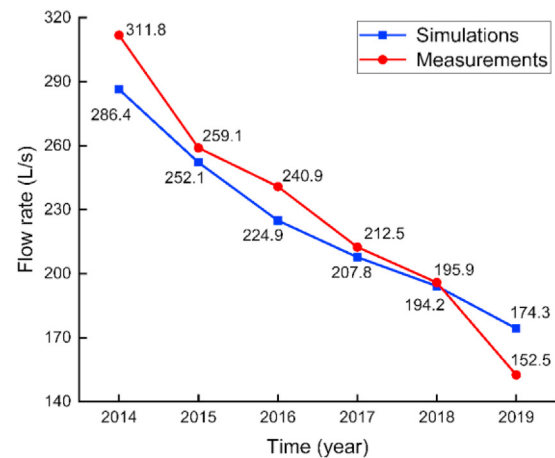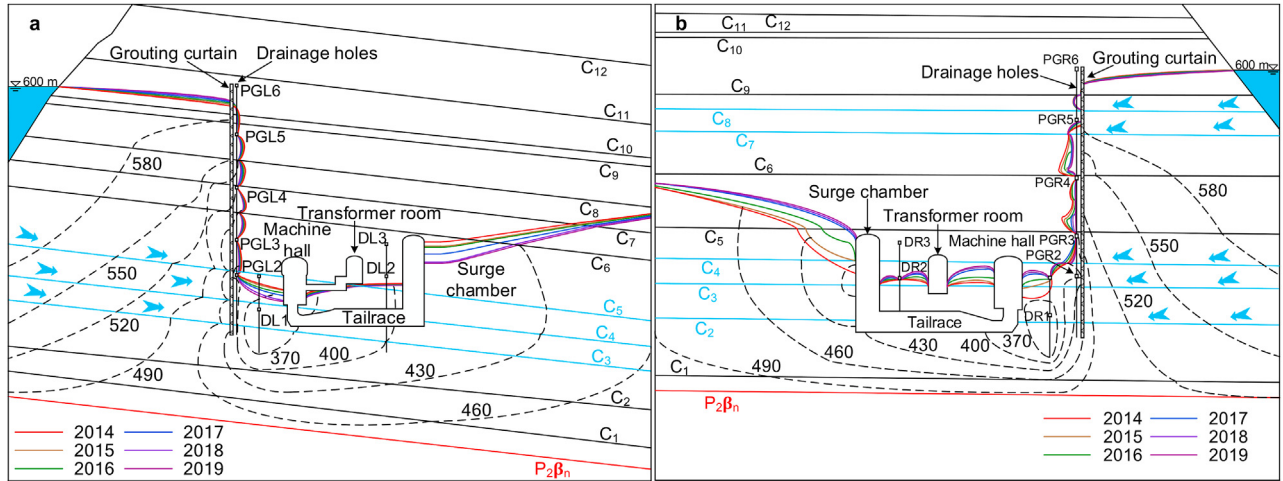

Fig. 15. Comparison between the measured and calculated total discharges at normal pool level (600 m) in early October annually.

Fig. 16. Hydraulic head contours (unit: m) and phreatic surface variations in the underground powerhouse areas: (a) along cross-section *A*–*A* in the left bank, and (b) along cross-section *B*–*B* in the right bank. The traces of the cross-sections are shown in Fig. 2.
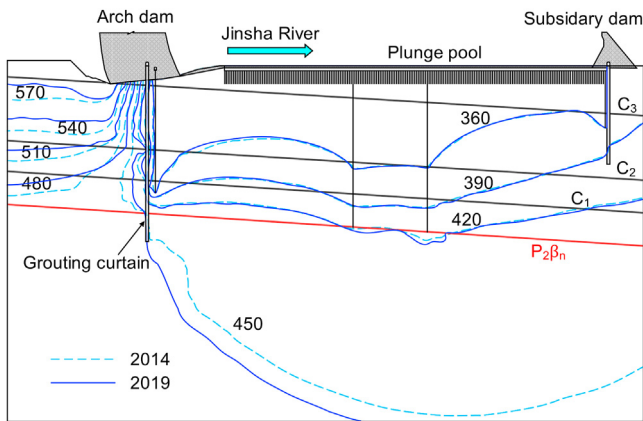
Fig. 17. Hydraulic head contours (unit: m) along the central cross-section *C*–*C* of the dam in early October of 2014 and 2019.

simulations with this permeability function well reproduce the groundwater flow behaviors at the site, and demonstrate the effectiveness of the complex seepage control system containing 7980 drainage holes and grout curtains covering an area of 8.7×10^5 m². The proposed permeability function is of great significance for long-term performance assessment of high dams over sediment-laden rivers because the permeability decay in foundation rocks reduces the pressure gradient in seepage-proof barriers, and this function could also be applicable for hyporheic exchange modeling, where the effect of fracture clogging on rock's permeability variation dominates.

Declaration of competing interest

The authors wish to confirm that there are no known conflicts of interest associated with this publication, and there has been no significant financial support for this work that could have influenced its outcome.

Nomenclature

d	Depth from ground surface
$\boldsymbol{e}_z$	Upwards vertical unit vector
H	Heaviside function
$\boldsymbol{K}, K$	Hydraulic conductivity tensor and its isotropic counterpart
$K_{//}, K_\perp$	Horizontal and vertical components of hydraulic conductivity
K_0, K_∞	Initial hydraulic conductivity and its asymptotic value after a sufficient long time; K_0 is also abused for hydraulic conductivity near the ground surface
M, N	Number of piezometers and weirs; N is also abused for the dimension of a time-series
$\boldsymbol{n}$	Outward unit vector to a boundary
$\boldsymbol{P}$	Vector of hydraulic parameters to be estimated
$\boldsymbol{Q}_j, \tilde{\boldsymbol{Q}}_j$	Time-series of calculated and measured discharges at weir j
$\bar{q}$	Prescribed flux on the flux boundary Γ_q
$\boldsymbol{R}, \boldsymbol{Z}$	Time-series of numerically obtained data and measurements at a monitoring point
S_s	Specific storage
t	Time
$\boldsymbol{v}$	Darcy velocity
w	Weight coefficient
z	Vertical coordinate
Γ_f, Γ_s	Free surface and potential seepage boundary
Γ_q, Γ_ϕ	Flux boundary and water head boundary
α, β	Fitting coefficients
ϕ	Total water head
$\bar{\phi}_0$	Initial distribution of water head
$\bar{\phi}$	Prescribed water head on the water head boundary Γ_ϕ

$\phi_i, \tilde{\phi}_i$ Time-series of calculated and measured water heads at piezometer i

μ Specific yield

ν Anisotropy ratio, $\nu = K_\perp / K_{//}$

References

Barlow, J.R.B., Coupe, R.H., 2012. Groundwater and surface-water exchange and resulting nitrate dynamics in the Bogue Phalia basin in northwestern Mississippi. J. Environ. Qual. 41 (1), 155–169.

Brunke, M., Gonser, T., 1997. The ecological significance of exchange processes between rivers and groundwater. Freshw. Biol. 37 (1), 1–33.

Brunke, M., 1999. Colmation and depth filtration within streambeds: retention of particles in hyporheic interstices. Int. Rev. Hydrobiol. 84 (2), 99–117.

Cao, Z.J., Zhang, X.B., Ai, N.S., 2011. Effect of sediment on concentration of dissolved phosphorus in the Three Gorges Reservoir. Int. J. Sediment Res. 26 (1), 87–95.

Carrera, J., 1993. An overview of uncertainties in modelling groundwater solute transport. J. Contam. Hydrol. 13 (1–4), 23–48.

Chen, C., Packman, A.I., Gaillard, J.F., 2008. Pore-scale analysis of permeability reduction resulting from colloid deposition. Geophys. Res. Lett. 35 (7), L07404. https://doi.org/10.1029/2007GL033077.

Chen, C., Lau, B.L.T., Gaillard, J.F., Packman, A.I., 2009. Temporal evolution of pore geometry, fluid flow, and solute transport resulting from colloid deposition. Water Resour. Res. 45 (6), W06416. https://doi.org/10.1029/2008WR007252.

Chen, C., Packman, A.I., Gaillard, J.F., 2009. Using X-ray micro-tomography and pore-scale modeling to quantify sediment mixing and fluid flow in a developing streambed. Geophys. Res. Lett. 36 (8), L08403. https://doi.org/10.1029/2009GL037157.

Chen, Y.F., Zhou, C.B., Sheng, Y.Q., 2007. Formulation of strain-dependent hydraulic conductivity for a fractured rock mass. Int. J. Rock Mech. Min. Sci. 44 (7), 981–996.

Chen, Y.F., Zhou, C.B., Zheng, H., 2008. A numerical solution to seepage problems with complex drainage systems. Comput. Geotech. 35 (3), 383–393.

Chen, Y.F., Zhou, C.B., Jing, L.R., 2009. Modeling coupled THM processes of geological porous media with multiphase flow: theory and validation against laboratory and field scale experiments. Comput. Geotech. 36 (8), 1308–1329.

Chen, Y.F., Hu, R., Zhou, C.B., Li, D.Q., Rong, G., 2011. A new parabolic variational inequality formulation of Signorini's condition for non-steady seepage problems with complex seepage control systems. Int. J. Numer. Anal. Methods GeoMech. 35 (9), 1034–1058.

Chen, Y.F., Hu, S.H., Wei, K., Hu, R., Zhou, C.B., Jing, L.R., 2014. Experimental characterization and micromechanical modeling of damage-induced permeability variation in Beishan granite. Int. J. Rock Mech. Min. Sci. 71, 64–76.

Chen, Y.F., Zheng, H.K., Wang, M., Hong, J.M., Zhou, C.B., 2015. Excavation-induced relaxation effects and hydraulic conductivity variations in the surrounding rocks of a large-scale underground powerhouse cavern system. Tunn. Undergr. Space Technol. 49, 253–267.

Chen, Y.F., Hong, J.M., Tang, S.L., Zhou, C.B., 2016. Characterization of transient groundwater flow through a high arch dam foundation during reservoir impounding. J. Rock Mech. Geotech. Eng. 8 (4), 462–471.

Chen, Y.F., Hong, J.M., Zheng, H.K., Li, Y., Hu, R., Zhou, C.B., 2016. Evaluation of groundwater leakage into a drainage tunnel in Jinping-I arch dam foundation in Southwestern China: a case study. Rock Mech. Rock Eng. 49 (3), 961–979.

Chen, Y.F., Ling, X.M., Liu, M.M., Hu, R., Yang, Z.B., 2018. Statistical distribution of hydraulic conductivity of rocks in deep-incised valleys, Southwest China. J. Hydrol. 566, 216–226.

Chen, Y.F., Yu, H., Ma, H.Z., Li, X., Hu, R., Yang, Z.B., 2020. Inverse modeling of saturated-saturated flow in site-scale fractured rocks using the continuum approach: a case study at Baihetan dam site, Southwest China. J. Hydrol. 584, 124693. https://doi.org/10.1016/j.jhydrol.2020.124693.

Cheng, L., Liu, Y.R., Yang, Q., Pan, Y.W., Lv, Z., 2017. Mechanism and numerical simulation of reservoir slope deformation during impounding of high arch dams based on nonlinear FEM. Comput. Geotech 81, 143–154.

Datry, T., Lamouroux, N., Thivin, G., Descloux, S., Baudoin, J.M., 2015. Estimation of sediment hydraulic conductivity in river reaches and its potential use to evaluate streambed clogging. River Res. Appl. 31 (7), 880–891.

Fan, Q.X., Zhou, S.W., Yang, N., 2015. Optimization design of foundation excavation for Xiluodu super-high arch dam in China. J. Rock Mech. Geotech. Eng. 7 (2), 120–135.

Fries, J.S., Trowbridge, J.H., 2003. Flume observations of enhanced fine-particle deposition to permeable sediment beds. Limnol Oceanogr. 48 (2), 802–812.

Gao, C., Xie, L.Z., Xie, H.P., He, B., Li, C.B., Wang, J., Luo, Y., 2017. Coupling between the statistical damage model and permeability variation in reservoir sandstone: theoretical analysis and verification. J. Nat. Gas Sci. Eng. 37, 375–385.

Grischek, T., Bartak, R., 2016. Riverbed clogging and sustainability of riverbank filtration. Water 8 (12), 604. https://doi.org/10.3390/w8120604.

Han, B., Xie, S.Y., Shao, J.F., 2016. Experimental investigation on mechanical behavior and permeability evolution of a porous limestone under compression. Rock Mech. Rock Eng. 49 (9), 3425–3435.

Harvey, J.W., Wagner, B.J., Bencala, K.E., 1996. Evaluating the reliability of the stream tracer approach to characterize stream-subsurface water exchange. Water Resour. Res. 32 (8), 2441–2451.

Hong, J.M., Chen, Y.F., Liu, M.M., Zhou, C.B., 2017. Inverse modelling of groundwater flow around a large-scale underground cavern system considering the excavation-induced hydraulic conductivity variation. Comput. Geotech. 81, 346–359.

Jain, A., Kumar, A.M., 2007. Hybrid neural network models for hydrologic time series forecasting. Appl. Soft Comput. 7 (2), 585–592.

Jiang, A.N., Liang, B., 2006. Nonlinear time series prediction model for dam seepage flow based on PSO-SVM. J. Hydraul. Eng. 37 (3), 331–335 (in Chinese).

Kelsall, P.C., Case, J.B., Chabannes, C.R., 1984. Evaluation of excavation-induced changes in rock permeability. Int. J. Rock Mech. Min. Sci. Geomech. Abstr. 21 (3), 123–135.

Kiel, B.A., Cardenas, M.B., 2014. Lateral hyporheic exchange throughout the Mississippi River network. Nat. Geosci. 7 (6), 413–417.

Li, D.F., Lu, X.X., Yang, X.K., Chen, L., Lin, L., 2018. Sediment load responses to climate variation and cascade reservoirs in the Yangtze River: a case study of the Jinsha River. Geomorphology 322, 41–52.

Li, J., Li, M.G., Chen, J.J., Xia, X.H., 2019. Theoretical study on influence of well clogging and variable injection pressure on seepage field induced by single-well recharge. Chin. J. Geotech. Eng. 41 (Supp.2), 226–229 (in Chinese).

Li, X., Chen, Y.F., Hu, R., Yang, Z.B., 2017. Towards an optimization design of seepage control: a case study in dam engineering. Sci. China Technol. Sci. 60 (12), 1903–1916.

Li, Y., Chen, Y.F., Jiang, Q.H., Hu, R., Zhou, C.B., 2014. Performance assessment and optimization of seepage control system: a numerical case study for Kala underground powerhouse. Comput. Geotech. 55, 306–315.

Mertes, L.A.K., 1997. Documentation and significance of the perirheic zone on inundated floodplains. Water Resour. Res. 33 (7), 1749–1762.

Mohamadi-Baghmolaei, M., Azin, R., Sakhaei, Z., Mohamadi-Baghmolaei, R., Osfouri, S., 2016. Novel method for estimation of gas/oil relative permeabilities. J. Mol. Liq. 223, 1185–1191.

Mooneyham, C., Strom, K., 2018. Deposition of suspended clay to open and sand-filled framework gravel beds in a laboratory flume. Water Resour. Res. 54 (1), 323–344.

Nowinski, J.D., Cardenas, M.B., Lightbody, A.F., 2011. Evolution of hydraulic conductivity in the floodplain of a meandering river due to hyporheic transport of fine materials. Geophys. Res. Lett. 38 (1), L01401. https://doi.org/10.1029/2010GL045819.

Packman, A.I., MacKay, J.S., 2003. Interplay of stream-subsurface exchange, clay particle deposition, and streambed evolution. Water Resour. Res. 39 (4), 1097. https://doi.org/10.1029/2002WR001432.

Pardoen, B., Talandier, J., Collin, F., 2016. Permeability evolution and water transfer in the excavation damaged zone of a ventilated gallery. Int. J. Rock Mech. Min. Sci. 85, 192–208.

Pusch, R., 1989. Alteration of the hydraulic conductivity of rock by tunnel excavation. Int. J. Rock Mech. Min. Sci. Geomech. Abstr. 26 (1), 79–83.

Rehg, K.J., Packman, A.I., Ren, J., 2005. Effects of suspended sediment characteristics and bed sediment transport on streambed clogging. Hydrol. Process. 19 (2), 413–427.

Rozemeijer, J.C., Van Der Velde, Y., McLaren, R.G., Van Geer, F.C., Broers, H.P., Bierkens, M.F.P., 2010. Integrated modeling of groundwater–surface water interactions in a tile-drained agricultural field: the importance of directly measured flow route contributions. Water Resour. Res. 46 (11), W11537. https://doi.org/10.1029/2010WR009155.

Sadhukhan, S., Dutta, T., Tarafdar, S., 2007. Simulation of diagenesis and permeability variation in two-dimensional rock structure. Geophys. J. Int. 169 (3), 1366–1375.

Santillán, D., Fraile-Ardanuy, J., Toledo, M.Á., 2013. Dam seepage analysis based on artificial neural networks: the hysteresis phenomenon. In: Proceedings of the 2013 International Joint Conference on Neural Networks (IJCNN). Institute of Electrical and Electronics Engineers (IEEE).

Shi, J., Lin, P., Zhou, Y.D., Wei, P.C., Wang, R.K., 2018. Reinforcement analysis of toe blocks and anchor cables at the Xiluodu super-high arch dam. Rock Mech. Rock Eng. 51 (8), 2533–2554.

Snow, D.T., 1969. Anisotropic permeability of fractured media. Water Resour. Res. 5 (6), 1273–1289.

Song, J.X., Chen, X.H., Cheng, C., Summerside, S., Wen, F.J., 2007. Effects of hyporheic processes on streambed vertical hydraulic conductivity in three rivers of Nebraska. Geophys. Res. Lett. 34 (7), L07409. https://doi.org/10.1029/2007GL029254.

Souley, M., Homand, F., Pepa, S., Hoxha, D., 2001. Damage-induced permeability changes in granite: a case example at the URL in Canada. Int. J. Rock Mech. Min. Sci. 38, 297–310.

Sun, Z.X., Zhang, X., Xu, Y., Yao, J., Wang, H.X., Lv, S.H., Sun, Z.L., Huang, Y., Cai, M.Y., Huang, X.X., 2017. Numerical simulation of the heat extraction in EGS with thermal- hydraulic-mechanical coupling method based on discrete fractures model. Energy 120, 20–23.

Tseng, F.M., Yu, H.C., Tzeng, G.H., 2001. Applied hybrid grey model to forecast seasonal time series. Technol. Forecast. Soc. Change 67 (2–3), 291–302.

Ulrich, C., Hubbard, S.S., Florsheim, J., Rosenberry, D., Borglin, S., Trotta, M., Seymour, D., 2015. Riverbed clogging associated with a California riverbank filtration system: an assessment of mechanisms and monitoring approaches. J. Hydrol. 529, 1740–1753.

Wieland, M., Kirchen, G.F., 2012. Long-term dam safety monitoring of Punt Dal Gall arch dam in Switzerland. Front. Struct. Civ. Eng. 6 (1), 76–83.

Zeng, J., Li, X., Ling, X.M., Yao, M.D., Lu, W.D., 2019. Rod elements method based on variational inequality approach of Signorini type for simulating drainage holes in seepage analysis. China Rural Water and Hydropower (10), 169–174 (in Chinese).

Zhou, C.B., Liu, W., Chen, Y.F., Hu, R., Wei, K., 2015. Inverse modeling of leakage through a rockfill dam foundation during its construction stage using transient flow model, neural network and genetic algorithm. Eng. Geol. 187, 183–195.

Zhou, J.Q., Chen, Y.F., Tang, H., Wang, L., Cardenas, M.B., 2019. Disentangling the simultaneous effects of inertial losses and fracture dilation on permeability of pressurized fractured rocks. Geophys. Res. Lett. 46 (15), 8862–8871.

Prof. Yi-Feng Chen received his PhD from Wuhan University, China in 2004, and has been professor at Wuhan University since 2009. He is associate editor of *International Journal of Rock Mechanics and Mining Sciences*, editorial board member of *Bulletin of Engineering Geology and the Environment*, editorial board member and scientific editor of *Journal of Rock Mechanics and Geotechnical Engineering*, and editorial board member of *Chinese Journal of Rock Mechanics and Engineering*. His research interests include complex flow behaviors (multiphase flow, non-Darcian flow, and Bingham fluid flow) and transport processes in fractured porous media, groundwater flow modeling and hydrogeological assessment in dam engineering, and coupled thermo-hydro-mechanical processes in geomaterials.